Journal of Nuclear Materials 503 (2018) 98–109

Contents lists available at ScienceDirect

Journal of Nuclear Materials

journal homepage: www.elsevier.com/locate/jnucmat

Determination of very low concentrations of hydrogen in zirconium alloys by neutron imaging

N.L. Buitrago [a], J.R. Santisteban [a, *], A. Tartaglione [a], J. Marín [a], L. Barrow [b], M.R. Daymond [b], M. Schulz [c], M. Grosse [d], A. Tremsin [e], E. Lehmann [f], A. Kaestner [f], J. Kelleher [g], S. Kabra [g]

[a] Centro Atómico Bariloche, CNEA-CONICET, Argentina
[b] Department of Mechanical and Materials Engineering, Queens University, Canada
[c] Technische Universitat Munchen, Heinz Maier-Leibnitz Zentrum, Garching, Germany
[d] Karlsruhe Institute of Technology, Germany
[e] Space Science Laboratory, University of California at Berkeley, USA
[f] Paul Scherrer Institut, Switzerland
[g] ISIS Facility, Rutherford Appleton Laboratory, UK

ARTICLE INFO

Article history:
Received 5 September 2017
Received in revised form
27 February 2018
Accepted 28 February 2018
Available online 3 March 2018

ABSTRACT

Zr-based alloys are used in nuclear power plants because of a unique combination of very low neutron absorption and excellent mechanical properties and corrosion resistance at operating conditions. However, Hydrogen (H) or Deuterium ingress due to waterside corrosion during operation can embrittle these materials. In particular, Zr alloys are affected by Delayed Hydride Cracking (DHC), a stress-corrosion cracking mechanism operating at very low H content (~100–300 wt ppm), which involves the diffusion of H to the crack tip. H content in Zr alloys is commonly determined by destructive techniques such as inert gas fusion and vacuum extraction. In this work, we have used neutron imaging to non-destructively quantify the spatial distribution of H in Zr alloys specimens with a resolution of ~5 wt ppm, an accuracy of ~10 wt ppm and a spatial resolution of ~25 μm × 5 mm x 10 mm. Non-destructive experiments performed on a comprehensive set of calibrated specimens of Zircaloy-2 and Zr2.5%Nb at four neutron facilities worldwide show the typical precision and repeatability of the technique. We have observed that the microstructure of the alloy plays an important role on the homogeneity of H across a specimen. We propose several strategies for performing H determinations without calibrated specimens, with the most precise results for neutrons having wavelengths longer than 5.7 Å.

1. Introduction

Zr alloys are widely used in nuclear power plants as nuclear fuel cladding and in pressure tubes in power plants (CANDU and RBMK). The coolant water at ~280°C-350 °C and ~90 bar slowly oxidizes the alloy; and part of the H resulting from the process enters into the Zr lattice as an interstitial atom. This produces a steady increase in the overall H concentration in the material with service time, embrittling the component and hence affecting its service life. In addition, over long operational periods, Zr alloy components can potentially degrade by a stress-corrosion cracking mechanism known as Delayed Hydride Cracking (DHC) [1]. DHC involves the diffusion of H from the bulk material into the stressed region ahead of a crack tip in response to a solubility gradient created by the stress field. As a result, there is a local increase in H concentration at the crack tip above the solubility limit, and the excess H precipitates as zirconium hydride. This is quickly followed by the rupture of the brittle hydride, which increases the length of the crack, and reinitiates the process. Crack growth can occur between room temperature and operation temperature, and crack velocity has a complex dependence on temperature, applied stresses, crack geometry and the thermal history of the component. This is because for hydrides to precipitate, H in solid solution must first diffuse from unstressed regions away from the crack into the crack tip, locally exceed the H solubility in the material and precipitate as zirconium hydride. Both the solubility and the diffusion coefficient of interstitial H in Zr alloys have an exponential dependence on temperature [2,3]. Besides this, hydrogen solubility depends on applied stresses, and

* Corresponding author.
E-mail address: j.r.santisteban@cab.cnea.gov.ar (J.R. Santisteban).

https://doi.org/10.1016/j.jnucmat.2018.02.048
0022-3115/

there is a clear thermal hysteresis between hydride dissolution and hydride precipitation.

In typical DHC tests, a constant load is applied to a pre-cracked specimen and the step wise crack growth is monitored by acoustical emission or potential drop techniques [4], followed by microscopic post-mortem examination. The possibility of visualizing H redistribution *in-situ* during DHC tests would allow a significantly clearer interpretation of the process, and provide direct quantification of many of the variables involved in DHC modelling. H solubility at operating temperatures ranges from 35 wt ppm H at 250 °C to 120 wt ppm H at 350 °C, which determines the extent of the concentration gradients appearing at each temperature. A sensitivity of ~5 wt ppm H would allow resolving concentration gradients with ~4% resolution at 350 °C and ~14% resolution at 250 °C. On the other hand, typical dimensions of DHC specimens are ~2×2 cm^2, which defines the minimal required field of view; whilst test times vary from several hours to hundreds of hours, depending on loading conditions, H contents and test temperatures. The precipitated hydride phase can be mapped in situ at such resolutions using synchrotron diffraction with time resolution of minutes [5,6], however in order to follow the progress of H within a sample at all temperatures, our goal is to provide spatial mapping of the total hydrogen content, including that in solution. Although determination of H in solution using synchrotron X-ray diffraction has also been reported [7,8], the technique is not directly applicable to DHC tests. This is because the method relies on measuring the shift of α-Zr peaks due to the presence of interstitial H, which in DHC tests will be very difficult to separate from the shift appearing due to the stress field surrounding the crack.

Diffusion coefficients of H in Zr alloys range from 2.7×10^{-11} m^2/s at 250 °C to 1.3×10^{-10} m^2/s at 350 °C but differences have been reported depending on microstructures [3] and specimen direction [9] (e.g, axial, radial and hoop for tubes, and rolling, transverse, and normal for plates). As a first application of this technique, in a separate work we have determined diffusion coefficients of H in different alloys, microstructures and directions [10]. For this we have used specimens of dimensions $10 \times 10 \times 4$mm^3, in order to represent the thickness of CANDU pressure tubes. The specimens have a ~200 μm thick hydride layer on one of their 10×10 mm^2 faces, hence upon isothermal heating a diffusion profile appears along the 4 mm thickness, perpendicular to the hydride layer. The diffusion profile can be effectively mapped by integrating the signal registered by many pixels at the same depth, hence gauging a much larger volume of material whilst keeping a fine resolution along the thickness direction. For this, we have adopted an effective pixel size of 5 mm along the direction perpendicular to the thickness, in order to define for such samples an effective *gauge volume* of 10mm × 5mm × 25 μm, which allows clear identification of the hydride layer and diffusion profiles within reasonable experimental times (~10 min). The requirements of those experiments have dictated the spatial resolution explored in the present work.

Neutron transmission experiments have long been used to quantify the H content within metallic specimens [11–15]. Essentially, the attenuation suffered by a collimated neutron beam as it passes through the specimen can render the bulk H content within it. This is because the beam attenuation in zirconium hydride is an order of magnitude larger than in most Zr alloys applied in nuclear installations. This large difference has been exploited to quantify H in Zr alloys by neutron imaging experiments, typically with a detection sensitivity limit of ~100 wt ppm of H [12,14], more than an order of magnitude larger than our present goal. Higher sensitivities (~10 wt ppm H) have been reported, but for very coarse spatial resolution ~10 mm [16,17]. Cold Neutron Prompt Gamma Activation Analysis is another non-destructive neutron based technique used to quantify Hydrogen pick-up in Zr alloys, with a sensitivity of ~5 wt ppm [18], but with no spatial resolution. The challenge of the present work is the optimization of the experimental arrangement and data analysis methodology in neutron imaging experiments, in order to achieve ~5 wt ppm sensitivity in H content coupled with a ~25 μm linear spatial resolution, whilst ensuring reasonably low acquisition times. Besides this, we aim to understand and quantify the effect of the different experimental variables on the experiment design in order to properly assess the resolution and accuracy of the technique.

2. Theory

In a typical neutron imaging experiment a horizontal, collimated, polychromatic neutron beam illuminates the specimen, and a two-dimensional plane detector is located behind the sample, perpendicular to the beam direction. The spatially resolved neutron transmission of the specimen $T(x,y)$ is measured by recording three images: the image I_s recorded with the sample in the beam, the image of the direct beam I_0, and the image B recorded with the beam blocked, in order to correct the other two images.

$$T(x,y) = \frac{I_s(x,y) - B(x,y)}{I_0(x,y) - B(x,y)}, \tag{1}$$

On a first approximation, the measured transmission depends on the sample thickness z (along the beam direction) and on the attenuation coefficient Σ

$$T(x,y) = \exp(-z(x,y)\Sigma(x,y,E)), \tag{2}$$

The spatial variation of both z and Σ is responsible for the contrast observed in the image. The attenuation coefficient is a property of the material that depends on neutron energy E, or equivalently on neutron wavelength λ, as shown in Fig. 1 for a metallic Zr alloy and for δ Zr hydride at room temperature ($ZrH_{1.67}$), the crystallographic hydride phase predominantly observed in pressure tubes and fuel cladding. The attenuation coefficients in the plot correspond to theoretical calculations, but they have been thoroughly compared to experimental results [19–22]. The mean attenuation coefficient of the hydride (~4 cm^{-1}) is ~16 times larger than the one for Zr alloys (~0.25 cm^{-1}), due to the incoherent scattering by H. Both attenuation coefficients present complex dependences on wavelength due to the effects of chemical binding. The sharp steps observed for both Zr alloys and hydrides at long wavelengths are due to neutron diffraction on crystal planes [23].

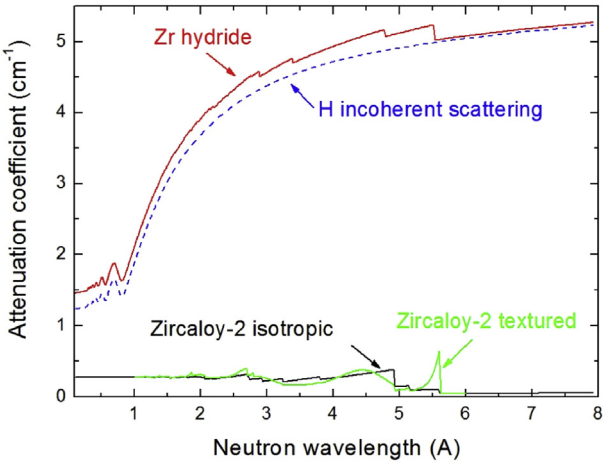

Fig. 1. Attenuation coefficient of Zirconium alloys [20] and zirconium hydride [22].

This *elastic coherent* contribution is of similar magnitude for both Zr alloy and hydride, yet the edges appear at different wavelengths due to the different crystal structures. The hydride attenuation is dominated by *incoherent scattering* by H, shown by the dotted blue line, which for $\lambda < 0.2$ Å presents a constant value corresponding to inelastic scattering by a nearly-free proton, and increases with wavelength with oscillations reflecting processes of energy exchanges with the optical vibrations of the proton within the crystal lattice [19]. For wavelengths $\lambda > 3$ Å the H attenuation has a strong dependence on temperature as a result of inelastic scattering process on which the neutron gains energy in the collision. The wavelength dependence of the incoherent contribution from individual H atoms (protons) is nearly the same for all hydride phases (γ, δ, ε). This is because the chemical binding is similar in all phases, with the protons occupying tetrahedral sites of the Zr sublattice. The largest variation in the attenuation coefficient between the three hydride phases comes from their difference in H density and, to a minor extent, on their elastic coherent contribution.

On the other hand, large variability is expected in the attenuation coefficient of Zr alloy specimens within the (2 Å-5.6 Å) wavelength range [24]. Within this range Σ_{Zr} depends on the crystallographic texture of the material, as this changes the numbers of crystal planes available for diffraction [20], and texture of a specimen is dependent on the specific manufacturing process. This is exemplified by comparing the attenuation of an isotropic specimen (solid black line) to that of a Zircaloy-2 tube along its axial direction (solid green line). Even for a single specimen, the details of the wavelength-dependent attenuation will depend on the angles the neutron beam makes with the principal axes of the specimen. Variations in alloy composition among specimens are usually not important, because composition is strictly controlled for nuclear-grade materials.

In order to define the precision required for the present experiments we estimate the attenuation coefficient for a Zr-alloy material containing a volume fraction of precipitated hydrides c_{HZr} as,

$$\Sigma(c_{HZr}, \lambda) = (1 - c_{HZr})\Sigma_{Zr}(\lambda) + c_{HZr}\Sigma_{HZr}(\lambda) \tag{3}$$

with Σ_{Zr} and Σ_{HZr} the attenuation coefficients of the Zr alloy and the hydride, respectively. For very small H contents the relative change in the transmission of a Zr-alloy specimen containing w_H ppm of H in weight as precipitated hydride is

$$\frac{T_{Zr} - T_{Zr+H}}{T_{Zr}} \approx c_{HZr} z(\Sigma_{ZrH} - \Sigma_{Zr}) \approx c_{HZr} z \Sigma_{H(ZrH)} = \frac{w_H\ [\text{ppm H}]}{17900} z \Sigma_{H(ZrH)} \tag{4}$$

where $\Sigma_{H(ZrH)} = \Sigma_{ZrH} - \Sigma_{Zr}$ is the H (incoherent)contribution to the attenuation coefficient of the hydride, e.g., the dotted-blue line in Fig. 1. In doing this, we have approximated the elastic coherent attenuation in ZrH by the corresponding attenuation in α-Zr. The value of 17900 wt ppm H corresponds to the composition of pure δ-Zr hydride at room temperature [1]. A content of H of 5 wt ppm corresponds to a hydride volume fraction of ~0.0003, so for a 1 cm thick sample we estimate a change in the specimen transmission in the order ~0.001, which dictates the precision required for the signal in the neutron imaging experiments. For larger H contents, the swelling of the specimen due to hydrogen uptake produces an increase in z that should also be considered in Eq. (4).

3. Samples

Samples were produced by the Department of Mechanical and Materials Engineering, Queens University, Canada. They consisted of twelve specimens of cold-rolled and recrystallized Zircaloy-2 and two specimens of hot-rolled Zr2.5%Nb, cathodically loaded with different H contents, and homogenized by annealing at 400 °C during 24 h. The microstructure of the materials is shown in Fig. 2 as observed in the optical microscope after standard polishing and etching procedures for Zirconium alloys [25]. Due to the almost zero solubility of H in Zr at room temperature, in all experiments hydrogen is present in the specimens in the form of micrometric precipitates of Zr hydride appearing as elongated plate-like clusters, which for the highest H contents can be as long as ~100 μm [26]. These hydrides are not observed in Fig. 2 as they offer no contrast for the chemical attack used to reveal the Zr grain structure.

All specimens had original dimensions of $10 \times 10 \times 4\text{mm}^3$. Preliminary measurements were performed on two facilities, and after that a ~$2.5 \times 10 \times 4$ mm^3 slice was cut from each sample to destructively determine the H content by hot vacuum extraction under the standard ASTM E 146-83. The resulting H contents and specimen lengths for all specimens are listed in Table 1.

In order to test the spatial resolution of the neutron technique, we produced two specimens, Zircaloy-2 and Zr2.5Nb of identical dimensions to the homogeneous specimens ($10 \times 10 \times 4\text{mm}^3$), but containing an inhomogeneous hydride distribution. These specimens contained a hydride layer on one of their 10×10 mm^2 faces, and were subsequently annealed at 250 °C for 10 h and 350 °C for 1.5 h, respectively, in order to create a H diffusion profile across the 4 mm thickness. These were the typical specimens of a companion experiment performed to determine H diffusion coefficients in different alloys [10].

4. Experiments

Neutron radiography experiments were performed at four instruments in facilities from Argentina, Switzerland, United Kingdom and Germany. The instruments have different characteristics as to the type of the neutron source and moderator material from which the neutrons emerge, the size D of the effective neutron source (pinhole diameter), the distance L between pinhole and sample, the incident flux on the sample, and the detection system (neutron sensitive material, spatial resolution). Table 2 lists the main features of the neutron imaging facilities used for this work, which are briefly described below. Preliminary measurements were performed on two cold neutron instruments (ICON at PSI-Switzerland, and ENGIN-X at RAL-UK), followed by a series of more detailed experiments on ENGIN-X at RAL-UK, and Antares at MLZ-Germany. For comparison, experiments were also performed on the thermal neutron imaging beamline of the RA-6 reactor, at CAB-Argentina.

Samples were placed in the neutron beam on different holders fabricated *ad hoc*, with steady improvements in design for simpler positioning and alignment and to reduce edge effects. The measurement of the direct beam consisted of removing the samples from the holder, while leaving the holder in place. On the preliminary measurements at ICON, the samples were placed in the neutron beam once at a time. After that experiment, samples were placed in the beam using the holders shown in Fig. 3, with the top row showing actual holders and specimens and the bottom row showing the corresponding neutron images. The initial designs aimed at maximizing the number of specimens that could be simultaneously imaged, in order to reduce experimental times. Fig. 3-(a) and 3-(b) show two bookshelf-type aluminium holders, used for the RA-6 and the preliminary ENGIN-X experiments, respectively. In the first case the specimen position is defined by a series of grooves on each horizontal shelf, whilst in the latter is defined by short segments of steel wire (~1 mm diameter) attached

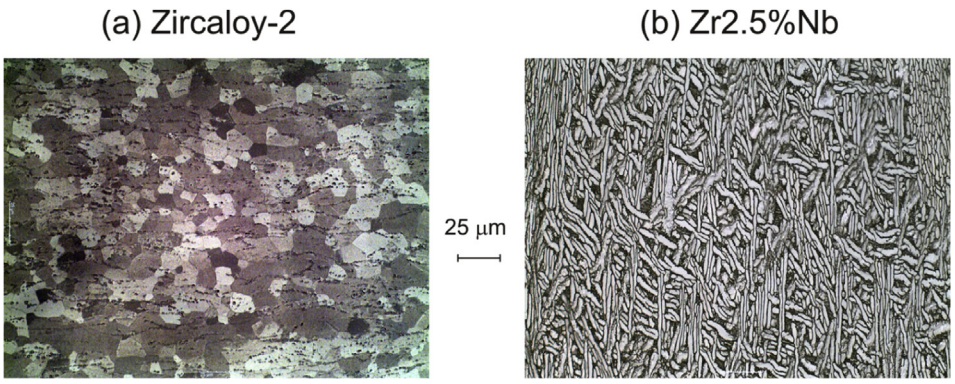

Fig. 2. Microstructures of the Zircaloy-2 and Zr2.5%Nb specimens. Hydrides are not observed as they offer no contrast for the chemical attack used to reveal the Zr grain structure.

Table 1
H content of the homogenous specimens determined by hot vacuum extraction (ASTM E 146-83). ZrNb refers to Zr2.5%Nb, while Zr2 refers to Zircaloy-2.

Sample	1	2	3	4	5	6	7	8	9	10	11	12	13	14
Material	ZrNb	Zr2	Zr2	Zr2	Zr2	Zr2	Zr2	Zr2	ZrNb	Zr2	Zr2	Zr2	Zr2	Zr2
Length (±0.1 mm)	7.3	7.3	7.4	7.2	7.4	7.6	7.3	7.5	7.3	7.4	7.4	7.4	7.1	7.3
H content (±5%)	7	11	14	26	37	58	64	84	130	166	171	175	248	366

Table 2
Main characteristics of the facilities used in the experiments.

Facility	Source	Moderator	Mean λ (Å)	Flux n cm^{-2} s^{-1}	L/D	Detector	Pixel size (mm)
EnginX	Spallation source	CH_4-110 K	~2	5×10^6	200	^{10}B doped microchannel plate	0.055
ICON	Spallation source	D_2-25 K	~4.5	1.3×10^7 mA^{-1}	450	Scintillator + CCD	0.013
Antares	FRM-II Reactor	D_2 -18 K	~1.8	6.4×10^7	500	Scintillator + CCD	0.02
RA-6	RA-6 Reactor	H_2O -293 K	~1.1	1.2×10^6	100	Scintillator + CCD	0.18

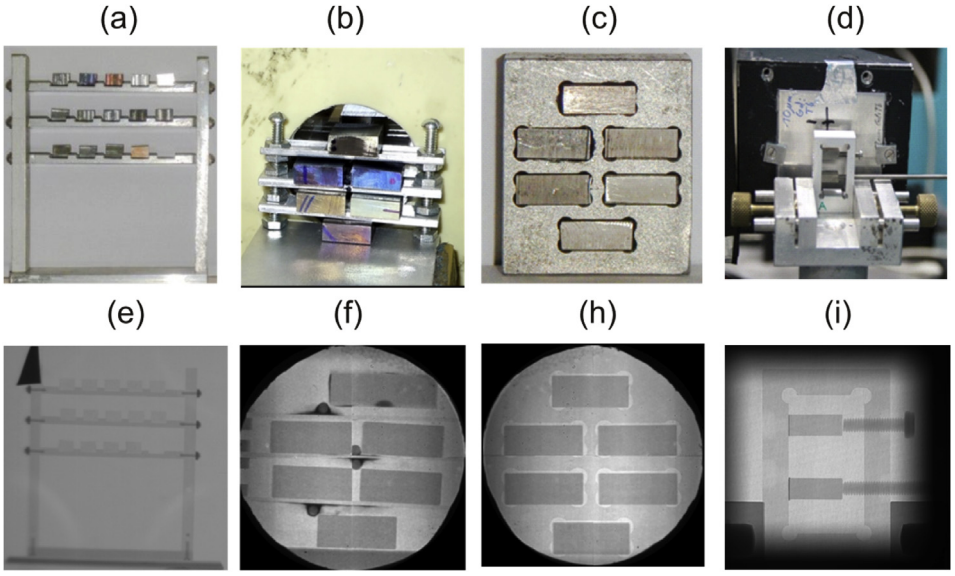

Fig. 3. Evolution of sample holders (top) and corresponding neutron images (bottom). (a) Used at RA-6 imaging beamline, (b) Used on preliminary tests on ENGIN-X, (c) Used for actual tests on ENGIN-X, (d) used on Antares. As a reference for all images, the horizontal dimension of the specimens is 10 mm.

to the shelf by super glue (the four dark features observed on the neutron image of Fig. 3-(f)). In order to improve positioning, the actual ENGIN-X experiments used the holder seen in Fig. 3-(c), consisting of a 10 mm thick aluminium plate with six grooved slots to place the specimens. However this design introduced large edge effect near surfaces due to total reflection at the Al-air-Zr interfaces, as discussed later. Hence, for the Antares experiments we used the holder in Fig. 3-(i), with a design aimed at reducing edge effects on the horizontal faces whilst improving specimen placement/removal and alignment. Only two specimens are measured per exposure, but this holder delivered the best repeatability and spatial resolution near the surfaces, important requirements for the

studies envisaged for this technique.

5. ANTARES

Experiments on this instrument are representative of the best performance that can be attained at leading neutron imaging facilities worldwide. The imaging beam line ANTARES at the FRM II reactor of the Maier-Leibnitz Zentrum, Germany, sees a liquid deuterium cold source at 18 K, with a variable collimator close to the reactor face, and two different detector positions in separate experimental chambers, at 9 m and 14 m from the pinhole [27]. This offers high flexibility to tailor resolution, flux, and field-of-view, depending on the requirements of each problem. In our experiment we used the 9 m position with an L/D of 500, and an ANDOR cooled CCD, with mirror and Gd_2O_2S scintillation screens of $40 \times 40\,mm^2$ and 20 μm thickness, 2048×2048 pixels, 16 bit, which gave a spatial resolution of ~20 μm. The incident spectrum has mean neutron wavelength of 2 Å and a flux of ~6.4×10^7 n cm^{-2} s^{-1} for L/D~500. For each specimen, 40 images of 10 s exposure were taken and later processed as described below.

6. RA-6 imaging beamline

As an example of the performance to be delivered by a low flux research reactor, experiments were performed at the imaging beamline of the RA-6 reactor in Centro Atómico Bariloche, Argentina (open-pool, 0.5 MW) [28]. A neutron beam with a thermal spectrum and direct view to the core is transported to the instrument through a conduct containing a sapphire filter and a conical collimator. A 4 cm pinhole gives L/D = 100 at the detector position at 4 m, and an incident spectrum with mean neutron wavelength of ~1.1 Å. Experiments were performed at 0.5 MW, with a thermal flux of 1.2×10^6 n/cm^2s, an epithermal flux of 3.8×10^3 n/cm^2s [28]. The detection system uses a $20 \times 20\,cm^2$, 0.5 mm thick scintillation plate (^{6}Li/ZnS:Ag) and a CCD camera (Penguin 600CLM), 1040×1392 pixels, with an effective pixel size of 180 μm and a dynamic range of 16 bits. Measurements consisted of 50 images with 20 s exposure. There are no beam limiters in the experimental area, so a large $25 \times 25\,cm^2$ area is illuminated during the experiments.

7. ENGIN-X

The dependence of the attenuation coefficient of the calibration specimens on neutron wavelength was measured on ENGIN-X, in order to assess the accuracy of the technique. ENGIN-X is a diffractometer at the ISIS Facility, UK, designed for the measurement of internal stresses using a pulsed neutron source [29]. ENGIN-X is not optimized for the acquisition of images, but it has ample space so it was possible to configure it to perform energy-resolved neutron imaging experiments using a detector developed by the Department of Space Sciences of the University of California at Berkeley [30]. The detector consists of a stack of ^{10}B doped micro-channel plates (MCPs), coupled to a single readout application-specific integrated circuit, that provides a pixel size of ~55 μm with a temporal resolution of ~1 μs. Each individual image is composed by 512×512 pixels, but the active area of the detector is a 28 mm diameter circle, as seen in Fig. 3-(f) and 3-(h).

At ISIS, short pulses of neutrons (~100 ns width) are created by bombarding a tungsten target with high-energy protons, 50 times per second. After passing through a liquid methane moderator, a polychromatic neutron beam travels along a 60 mm high x 25 mm wide, curved, neutron guide to illuminate the sample in the ENGIN-X instrument, located at ~50 m from the moderator. The area detector placed just behind the sample registers both the position and time where the neutrons are detected. In this way, neutron images of the specimen are produced at different times, counted from the initial time t_0 when the original neutron pulse is produced. As neutrons of different energies take different times to arrive at the detector, each image, taken for a specific time interval relative to the start time of the proton pulse, reveals the transmission through the specimen for neutrons within a precise energy (or wavelength) range. The time-of-flight (TOF) that a neutron spends travelling the distance L from the moderator to the detector is proportional to its wavelength λ, TOF = $mL\lambda/h$, where m is the neutron mass and h the Plank constant. Due to the low integral fluxes of pulsed neutron beams (as compared to reactor sources) each wavelength-resolved radiographic image is produced by adding the counts registered after several thousands of neutron pulses. For each experimental arrangement, images were taken at 2930 different TOF intervals of 28 μs width, centered at TOFs between 10 μs and 98000 μs. Each image included the counts after ~35000 proton pulses, giving typical counting times of one hour per arrangement.

8. ICON

Preliminary measurements were performed on this beamline, also representative of the best performance attained worldwide. The cold neutron imaging instrument ICON is a versatile beamline specialized on high resolution and small samples [31], located at the Spallation Neutron Source SINQ, a continuous source at the Paul Scherrer Institut, Switzerland. Starting from the source the neutrons are collected by a channel with a square cross-section and after a shutter, it has an aperture system made of steel with six exchangeable apertures, with diameters of 1, 10, 20, 40, and 80 mm, and an additional 20 mm aperture with a beryllium filter inserted. The Be filter can be used to suppress higher energy neutrons from the beam. Vacuum flight tubes are installed between the experimental shutter and the experimental positions to avoid loss of neutrons due to scattering in air. The flight tubes are divided into three independent segments. This allows for convenient changes between measurement positions without breaking vacuum. We used the second experimental position with the Be filter, and L/D of ~450 and a flux of 1.3×10^7 n cm^{-2} s^{-1} mA^{-1}, with a $27 \times 27\,mm^2$ ^{6}Li/ZnS:Ag-based scintillator screen and a digital camera Andor DV436 composed of 2048×2048 pixels with a pixel size of 13 μm.

9. Data analysis

For the proposed method to be successful the images I_S, I_0 and B must be measured with a statistical uncertainty good enough to define the transmission T with a sensitivity of half of the required resolution of ~0.1%. Assuming Poisson statistic, a single detection unit (e.g., a single pixel or groups of pixels) registering n neutron counts has a relative uncertainty $\Delta n/n = n^{1/2}$; so a minimum of ~4×10^6 neutron counts per detection unit with the sample in place should be registered for the desired resolution. The limited effective dynamical range and sensitivity to spurious events of the detection system do not allow this number of counts to be recorded in a single measurement, so several images N_i (e.g., N_S, N_0, N_B) needed to be taken, and statistically processed to achieve this resolution. Moreover, in order to calculate the transmission T, the neutron flux is obtained by normalizing the registered counts by the measuring time Δt per individual image, and by the pixel area $\Delta x \Delta y$. Hence quantitative flux images used for calculations correspond to:

$$\tilde{\varphi}_{0,S,B}(x,y) = \frac{\langle I_{0,S,B}(x,y)\rangle_{N_{0,S,B}}}{\Delta x \Delta y \Delta t} \quad (5)$$

where $\langle\ldots\rangle_N$ stands for the statistical averaging over the N images taken in each case. For RA-6 and Antares (based on scintillation plates coupled to CCD cameras), $\langle\ldots\rangle_N$ stands for the median of each image group, as this magnitude is less sensitive to so-called "white spots", sporadic events that saturate individual pixels. For ENGIN-X, $\langle\ldots\rangle_N$ stands for the sum of the images recorded for all TOFs, divided by the TOF channel width and the number of accelerator pulses. No averaging was done on the preliminary ICON measurements, as only one image was taken for each specimen.

The transmission image of each specimen was evaluated from the $\tilde{\varphi}_{0,S,B}(x,y)$ images using Eq. (1). From this transmission, an experimental attenuation coefficient was evaluated as

$$\tilde{\Sigma}(x,y) = \frac{-\ln \tilde{T}(x,y)}{z} = \frac{-\ln\left(\frac{\tilde{\varphi}_S(x,y)-\tilde{\varphi}_B(x,y)}{\tilde{\varphi}_0(x,y)-\tilde{\varphi}_B(x,y)}\right)}{z} \quad (6)$$

For all instruments, images were produced using a polychromatic neutron beam with a thermal or cold neutron spectrum, so such attenuation coefficient corresponds to a (weighted) average of the values presented in Fig. 1, as discussed in section *Discussion*.

In many cases line profiles of T or $\tilde{\Sigma}$ have been evaluated, for better comparison of the results obtained at different facilities, or between different specimens. In such cases, spatial resolution has been relaxed on the direction perpendicular to the line profiled in order to improve statistics or sampling volume. Here, all statistical and binning operations were performed using the open source software ImageJ, and custom-written Matlab™ codes.

10. Results

Fig. 4 shows the transmission profiles obtained for the specimen containing 14 ppm H at all facilities. The profile corresponds to the yellow line indicated in the inset, which is a 90°-rotated detail of the normalized image taken at Antares, obtained from the image presented in Fig. 3-(i). Each point in the profile integrates the counts registered along a 4 mm long slice perpendicular to the yellow line, so the total area explored by the profile corresponds to the shaded area of the inset. These profiles show that the behavior at the edges of the specimen (indicated by black dotted vertical lines) is very dependent on the details of the experimental arrangement. Total reflection is observed on the air side at the Zr-air interfaces, producing transmission values larger than one over such regions. Refraction on the specimen side produces a rapid change in transmission near the surface. Because of this, the edge region must be ignored, and the actual information about the specimen is contained in the flat region in the interior of the specimen, far from the edges. The value of the transmission of the specimen within this region depends on sample thickness, H content of the specimen, the incident neutron spectrum and the spectral efficiency of the detection system.

Regarding edge effects, they were enhanced in ENGIN-X by the use of the aluminium sample holder of Fig. 2-(c) because both the Zr-air and Al-air interfaces reflected neutrons contributing to the peak observed at ~4 mm, whilst the effect is not observed at the Zr-Al interface at 0 mm, due to the similarity on the neutron refraction index of both materials. As seen in the figure, the effect is symmetrical and considerably smaller for the Antares experiments due to the improved design of the holder. Reflection is not observed in RA-6 due to the hotter spectrum and poorer collimation of the beam.

After the preliminary experiments, the Antares experiments were performed by a measurement strategy optimized to achieve the required statistical uncertainty, and maximize the usable region of the specimen. By using the holder of Fig. 3-(i) and taking 40 images of each specimen, we could measure up to 150 μm from the surfaces with a typical statistical uncertainty in the measured transmission at pixel level of 0.4%, which improves to a value of 0.02% for the line profiles.

The sensitivity of the neutron imaging technique to H content can better be assessed in terms of the attenuation coefficient $\tilde{\Sigma}$, as this accounts for small variations in transmission that arise due to differences in thickness among the specimens. Fig. 5 shows line profiles of $\tilde{\Sigma}$ for selected specimens measured in Antares, over the usable region indicated in the neutron images at the right of the figure. The figure includes results for two Zircaloy-2 homogeneous specimens (11 and 171 wt ppm H), one Zr2.5%Nb homogeneous specimen (130 wt ppm H), and the two Zircaloy-2 inhomogeneous specimens, annealed at 350 °C and 250 °C. For the homogeneous specimens, each solid square symbol is sampling $\tilde{\Sigma}$ over a volume of $\sim 7.5 \times 4 \times 0.02\ \mathrm{mm}^3 = 0.6\ \mathrm{mm}^3$ with a statistical uncertainty of

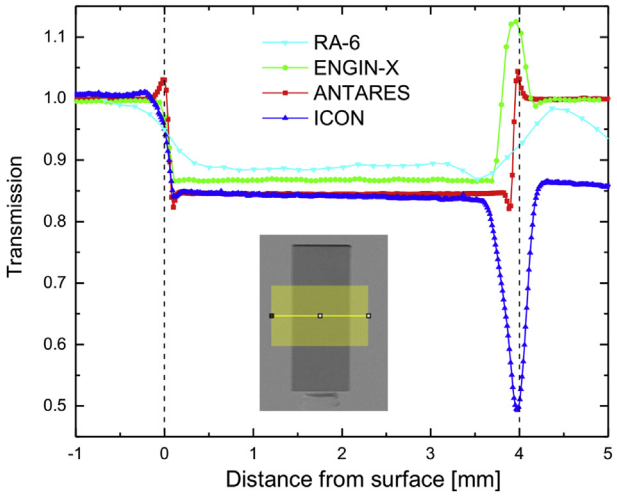

Fig. 4. Transmission profile of the specimen of Zircalloy-2 containing 14 wt ppm H, measured at the different neutron imaging facilities. The different effects observed at the edges are due to the use of different sample holders, shown in Fig. 3. The width of edge effects reflects the spatial resolution of the measurement.

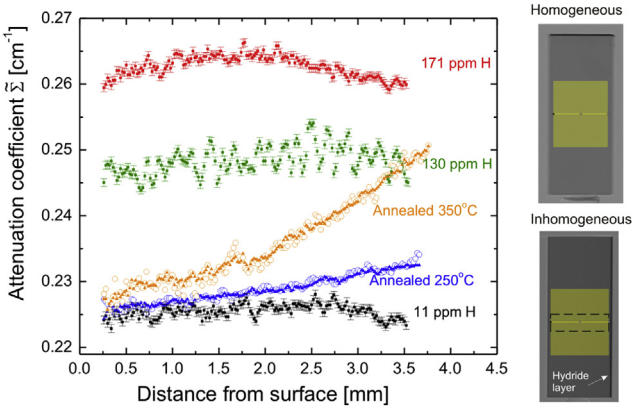

Fig. 5. Profile of the attenuation coefficient across the thickness of the homogenous and inhomogeneous specimens measured at Antares, along the yellow line indicated in the insets. The volume of material sampled by the profiles is indicated by the yellow-shaded areas. (For interpretation of the references to colour in this figure legend, the reader is referred to the Web version of this article.)

~0.0006 cm^{-1}. The overall H content of the homogeneous specimens can be easily discriminated, as they appear at well separated $\tilde{\Sigma}$ values. The local variations in $\tilde{\Sigma}$ found within each specimen can also be ascribed to differences in H content, as the size of hydride clusters can be comparable to the smaller dimension of the gauge volume (0.02 mm). The influence of microstructure on this effect is clear, as local variations are considerably larger for Zr2.5%Nb containing (130 ± 7)wt ppm H than for Zircaloy-2 containing (171 ± 9) wt ppm H. This suggests a much coarser, uneven distribution of hydrides for the microstructure shown Fig. 2-(b). The homogeneous specimens also reveal small variations in the overall distribution of H across the specimen, an effect most noticeable for the Zircaloy-2 specimen containing 171 wt ppm H. A higher attenuation coefficient is observed at the centre of the specimen, which indicates lower H concentrations near the surfaces.

The profiles obtained for the annealed, inhomogeneous specimens show the capability of neutron imaging to resolve concentration profiles within the 0–100 wt ppm H range, with a spatial resolution of ~25 μm (in one dimension). In this case, each small solid triangular symbol has the same sampling volume as for the homogenous specimens (~$7.5 \times 4 \times 0.02\ mm^3 = 0.6\ mm^3$), whilst each large open circular symbol is sampling a smaller volume of ~$7.5 \times 1 \times 0.02\ mm^3 = 0.15\ mm^3$). The smoother profile obtained for the specimen annealed at 250 °C is due to its specific microstructure (fewer hydride clusters) and better statistics, as 164 images were taken for this specimen, instead of 40 as for the other specimens. After conversion to H content, a quantitative analysis of the inhomogeneous profiles allows determination of the diffusion coefficient of H in the alloy at the annealing temperature [10].

In order to calibrate the technique and assess its resolution and repeatability, Fig. 6 compiles the mean attenuation coefficient $\tilde{\Sigma}$ measured for all homogeneous specimens as a function of the H content determined by hot vacuum extraction. The measurement is over a $7 \times 2\ mm^2$ area in the center of the specimen. Solid and open symbols are used for Zircaloy-2 specimens and Zr2.5%Nb specimens, respectively. Measurements performed at each facility are identified by the symbol shape. Results from all facilities show very good correlation between $\tilde{\Sigma}$ and the H content determined by hot vacuum extraction. The figure also includes calibration lines, with solid and dotted lines corresponding to Zircaloy-2 and Zr2.5%Nb specimens, respectively. Calibration lines for Zircaloy-2 have been obtained by linear regression to the data. As only two Zr2.5%Nb specimens were measured, in this case the calibration line has been produced by adjusting the ordinate by least-squares fit to the data, whilst keeping the slope fixed to the value obtained for Zircaloy-2 on each facility.

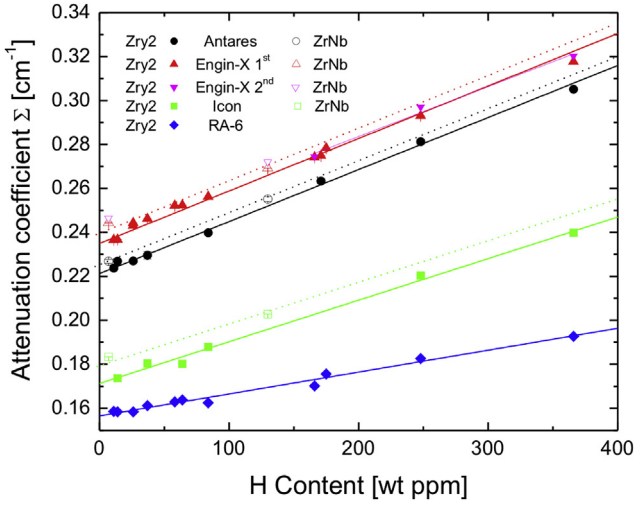

Fig. 6. Calibration lines between attenuation coefficient of the homogeneous specimens and H content determined by hot vacuum extraction, obtained for all facilities.

Table 3 Lists the slope ($d\tilde{\Sigma}/dH$), the ordinate ($\tilde{\Sigma}_0$), and the standard deviation of the data from the calibration line ($\delta\tilde{\Sigma}$) obtained for the Zircaloy-2 specimens for all experiments, together with the uncertainties reported by the least-squares fitting procedure.

The sensitivity of the technique is directly given by the slope of the calibration line. The sensitivity is nearly identical ($0.00021 \pm 0.00002\ cm^{-1}$/wt ppm H) for all the cold facilities visited here, and nearly twice of the value found at the thermal source (~$0.0001\ cm^{-1}$/wt ppm H). The values agree well with the calibrations given in Ref. [32]. The resolution e.g., the smallest increment in H content that can be determined depends mainly on the choice of instrument and utilized wavelength band, the number of images recorded and the counting time per image. It can be estimated by:

$$\Delta H = \frac{\delta\tilde{\Sigma}}{d\tilde{\Sigma}/dH}, \tag{7}$$

with $\delta\tilde{\Sigma}$ is the standard deviation of the data from the calibration line. The estimated resolution for the present experiments is also reported in Table 3. The highest resolution (~5 wt ppm H) is achieved for the optimized experiments performed in Antares, yet a very reasonable resolution (~18 wt ppm H) is also obtained for the preliminary experiments at ICON, with only one image registered per specimen. It is also worth noting that a reasonable resolution (~16 wt ppm H) is also obtained at RA-6, a relatively small research reactor. On the other hand, the ordinate $\tilde{\Sigma}_0$ measured for RA-6, 0.1567 cm^{-1}, is considerably smaller than the value expected from a theoretical estimation, ~0.25 cm^{-1}. This may be due to a contribution of neutrons not traversing the sample into the registered signal, due to scattering on the walls and equipment of the large beam used in these studies, as well as to incoherent scattering in the specimens.

The repeatability of the technique has been very good for all dedicated neutron instruments. In Antares measurements on the same specimen on two different days were within 0.12%. As observed in Fig. 6, repeatability was also very reasonable for ENGIN-X where the whole detection system is mounted and dismounted *ad hoc*, as attenuation coefficients measured at the two visits to the instrument (separated by seven months) agree within 0.7%.

We have used the calibration obtained for Antares to produce images of H content for the two inhomogeneous specimens, as shown in Fig. 7. On doing this, we have assumed that the calibration line obtained for the bulk of sample and detector can be directly applied for each individual pixel. Due to the larger statistical uncertainty in $\tilde{\Sigma}$ at pixel level, the uncertainty in H content of the images is considerably larger than 5 wt ppm H. With uncertainty in $\tilde{\Sigma}$ at pixel level being ~0.005 cm^{-1} and ~0.0035 cm^{-1} for the specimens annealed at 350 °C and 250 °C, respectively, uncertainties in H content are ~30 wt ppm H and ~20 wt ppm H for the respective images of Fig. 7. The line profiles of H content obtained from the data presented in Fig. 5 are shown on the right of each image. A resolution of ~5 wt ppm H with a spatial resolution of ~25 μm normal to the surface and 3.6 mm parallel to the surface is reported for these profiles.

Table 3
Parameters of the calibration lines obtained for each facility.

Instrument	Slope $d\bar{\Sigma}/dH$ (cm^{-1}/wt ppm H)	Ordinate $\bar{\Sigma}_0$ (cm^{-1})	Standard deviation $\delta\bar{\Sigma}$ (cm^{-1})	Resolution (wt ppm H)
Antares	$(2.30 \pm 0.04)10^{-4}$	0.2219 ± 0.0008	0.0012	5
Engin-X 1st	$(2.2 \pm 0.2)10^{-4}$	0.238 ± 0.005	0.003	14
Engin-X 2nd	$(2.25 \pm 0.05)10^{-4}$	0.237 ± 0.001	0.0018	8
ICON	$(1.9 \pm 0.1)10^{-4}$	0.172 ± 0.002	0.0034	18
RA-6	$(0.98 \pm 0.04)10^{-4}$	0.1567 ± 0.0007	0.0016	16

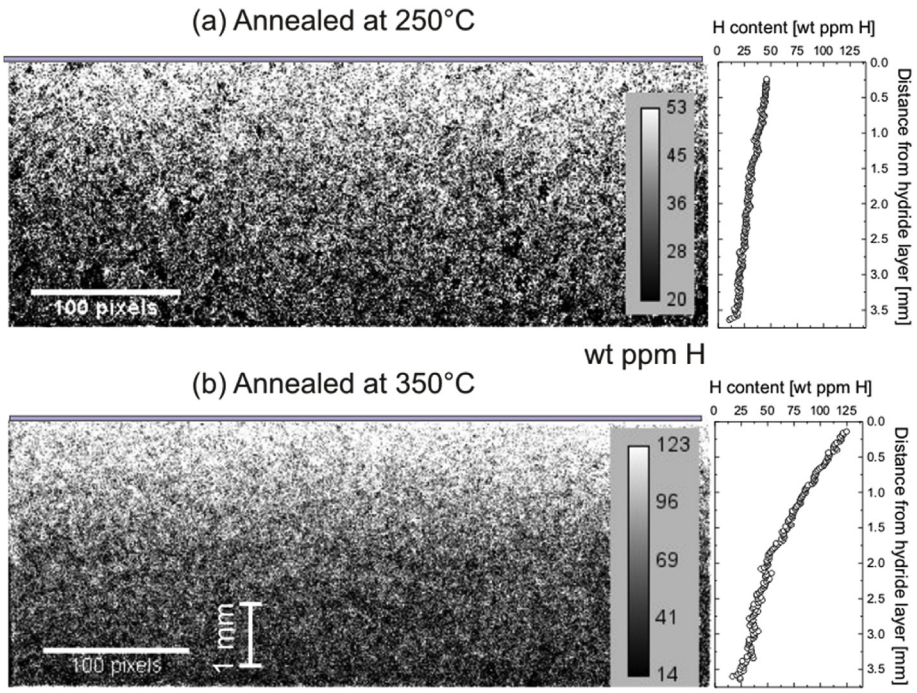

Fig. 7. Left: Images of H content in the two inhomogeneous specimens measured in Antares. Typical uncertainties in the images are ~30 wt ppm H and ~20 wt ppm H for the specimens annealed at 350 °C and 250 °C, respectively. Spatial resolution is ~25 μm and counting times are 164 × 10s (top) and 40 × 10s (bottom). Right: H concentration profile, averaging the values over horizontal lines 180 pixels long. Typical uncertainty is ~5 wt ppm H.

11. Discussion

11.1. Resolution and accuracy

In this work it was shown that neutron imaging experiments can be effectively used to map distributions of *low* H concentration occurring in Zr alloys, within the range of 1–300 wt ppm H. This expands the application range of the neutron imaging technique, which has been previously used for concentrations in the range ~500–10000 wt ppm H [14,15,32]. The *sensitivity* of the neutron imaging technique to H content depends mainly on the energy spectrum of the neutron beam, as it was observed from the slopes of the calibration lines presented in Table 3. The spatial resolution of the technique depends mostly on the beam collimation, which is usually coarser than the spatial resolution of the associated detection system. Current spatial resolution for state-of-the art instruments is ~20 μm, but on course developments aim at ~5 μm [33]. This requires measuring the sample in close contact to the detector, in order to reduce the effect of the beam divergence on resolution.

On the other hand, the *resolution* of the technique is defined by the precision of the measured values of H content, which depend mostly on two aspects: (i) the statistical uncertainty of the measurement, and (ii) the capability to perform a precise calibration between the measured property (the experimental attenuation coefficient given in Eq (6)) and the real amount of H contained within the gauge volume sampled by the neutron beam. Regarding (i), we have corroborated that the statistical uncertainty of the data must be as good as estimated, 0.1% for samples of ~10 mm thickness. Measurement of a thinner specimen will require a lower uncertainty, directly proportional to the thickness as seen from Eq. (4). The measuring time required to obtain this statistical resolution is achieved by taking the same image many times (~40 times for 10 mm thick specimens, giving a total time of ~400 s), and producing the median of such images. The need to record many images increases experimental times and prevents some *in-situ* studies of processes. Hence, another option to achieve the required uncertainty consists on relaxing the spatial resolution of the system by grouping the counts registered by several pixels, as presented in Fig. 5.

In order to calibrate the technique we have compared the measured attenuation coefficients to the values of H content reported by the (destructive) hot vacuum extraction technique (ASTM E 146-83), on 2.5 mm slices taken from each of the calibration specimens, with a typical accuracy of ~5% of the reported values (Table 1), which results in ~8 wt ppm H for a typical specimen containing 130 wt ppm H. So, an implicit assumption was made in our calibration, e. g., that H distribution in the original specimens was homogeneous within ~8 wt ppm H. On a broad scale, this is confirmed by the images and profiles of attenuation coefficient for

the homogeneous specimens shown in Fig. 5, and the good correlation between the measured overall attenuation coefficients and the H content obtained from hot vacuum extraction of Fig. 6. A closer inspection of Fig. 6 shows that the attenuation coefficient measured in all four facilities for the specimen containing the highest H content (366 wt pm H) is consistently below the adjusted calibration line, whilst the next two specimens (248 and 175 wt ppm H) are consistently above the calibration line (with the exception of the 248 wt ppm H specimen for the first visit to Engin-X). Such difference could be due to:

(i) small, real, differences in the actual H content of the specimens measured by neutron imaging and those measured by hot vacuum extraction,
(ii) small differences in the attenuation coefficient of the Zr alloy material,
(iii) small uncertainty in the thickness of the specimen (~50 μm).

Fig. 5 indicates that small local variations in H content do exist within the samples, and that the range of such variation depends both on the material and the overall H content. On the other hand, Fig. 8 shows the experimental wavelength-dependent attenuation coefficient of the ZrNb calibration specimen containing 130 wt ppm H measured on Engin-X, along two perpendicular directions of the specimen. The clear differences between measurements observed on the 2 Å-5.5 Å range are due to the crystallographic texture of the material, and will result in small differences in the average experimental attenuation defined in Eq. (6). This effect was not anticipated during the production of the calibration specimens, so they were produced having a square section of $10 \times 10\,mm^2$ without track of the relevant manufacturing directions of the specimen (rolling and transverse directions). So, specimens may have been indistinguishably measured along either of the two directions. The uncertainty in the thickness of the specimens may also be responsible for the observed deviations. Whatever the reason for these real, small, departures from the calibration line, we consider that a resolution of ~5 wt ppm H seems to be indeed the highest precision to be achieved by the calibration procedure adopted here, based on the information provided by hot vacuum extraction tests.

Regarding calibration for different alloys, Fig. 6 shows a systematic upward shift in the attenuation coefficient measured in all facilities for the Zr2.5Nb specimens, as compared to the Zircaloy-2 specimens. This may be due to differences in texture or composition between the two alloys. This was accounted for in the calibration for ZrNb, by adopting calibration lines (dotted lines) with the same slope measured for Zircaloy-2 but with a different ordinate. This assumption is based on the fact that the attenuation coefficient of zirconium hydride (Fig. 1) remains essentially the same for the different alloys [34]. So, in practice, in order to produce the calibration line for a specific alloy it would be enough to define the ordinate by measuring the attenuation coefficient of a single specimen of the material without H in it, and adopt the slope determined for any other Zr alloy.

Regarding the slopes listed in Table 3 it is interesting to note that the values measured for the three cold neutron beams used here are within a ±10% range ($0.00021 \pm 0.00002\,cm^{-1}$/wt ppm H), despite the fact that such value could in principle present larger variations due to differences in incident neutron spectra and detector efficiencies.

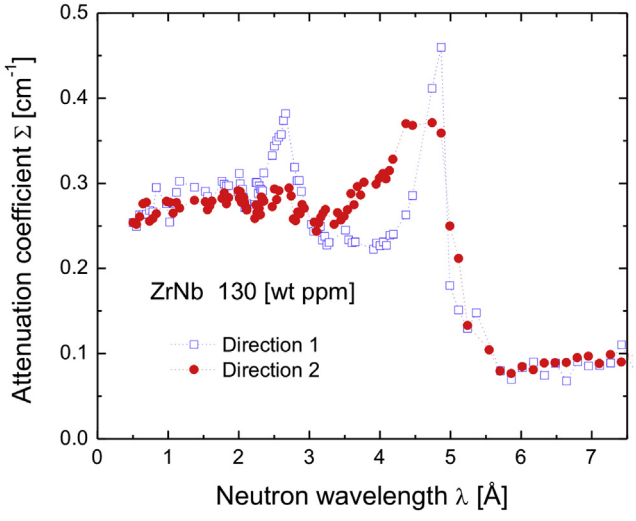

Fig. 8. Attenuation coefficient of the Zr2.5%Nb calibration specimen containing a homogeneous content of 130 wt ppm H measured along two perpendicular directions on Engin-X. The differences observed between 2 Å and 5.5 Å are due to the crystallographic texture.

11.2. Absolute calibration

Besides the limitation in the effective resolution achievable by the calibration procedure adopted here (~5 wt ppm H), the production of calibrated specimens is a time-consuming and expensive process. So, it is in principle attractive to be able to evaluate the calibration lines from theoretical grounds and the wavelength-resolved neutron spectrum registered by the detector system. Hence, we have theoretically evaluated the dependence of the wavelength-averaged attenuation given in Eq (6) on H volume fraction as:

$$\tilde{\Sigma}(c_H) = \frac{-1}{z} \ln \left(\frac{\int_{\Delta\lambda} \varphi_0(\lambda) \exp(-z\Sigma(c_H,\lambda)) d\lambda}{\int_{\Delta\lambda} \varphi_0(\lambda) d\lambda} \right) \tag{8}$$

where $\phi_0(\lambda)$ is the wavelength-dependent neutron spectrum registered by the detector system with no sample on the beam (e.g., I_0), normalized by counting time and area, over the wavelength interval of interest $\Delta\lambda$, and $\Sigma(c_H,\lambda)$ has been defined in Eq (3). The value of $\phi_0(\lambda)$ can be calculated, or experimentally determined using either a pulsed source or a device to monochromatize the neutron beam. Fig. 9 shows the neutron spectra measured on Engin-X using the pixelated MCP detector over an area of 2×7 mm^2 without the sample in the beam (black solid squares, ϕ_0) and with the sample in the beam (open red circles, ϕ_S).

We have evaluated the calibration lines from Eq. (8) using $\phi_0(\lambda)$ presented in Fig. 9 and Eq. (3) for $\Sigma(c_H,\lambda)$, with un-textured models for the attenuation coefficient of the Zr alloy ($\Sigma_{Zr}(\lambda)$) and the hydride ($\Sigma_{HZr}(\lambda)$) (black and red lines on Fig. 1, respectively). The resulting value for the slope, $d\tilde{\Sigma}/dH = 2.1 \times 10^{-4}\,cm^{-1}$/wt ppm H, agrees well with the experimental value reported on Table 3, whilst the ordinate $\tilde{\Sigma}_0 = 0.261\,cm^{-1}$ presents a small but important difference to the experimental value, as this would result in a systematic shift of ~28 wt ppm H on the resulting values of H content. This difference is likely to be due to an imprecise description of the attenuation coefficient of the Zr lattice, as possible texture effects such as those revealed by Fig. 8 in the 2 Å-5.5 Å range are not considered in the model. This is partially confirmed by Fig. 10, showing the wavelength-dependent attenuation coefficient of selected Zircaloy-2 calibration specimens measured on Engin-X over an area of 2×7 mm^2 (open symbols), together with the

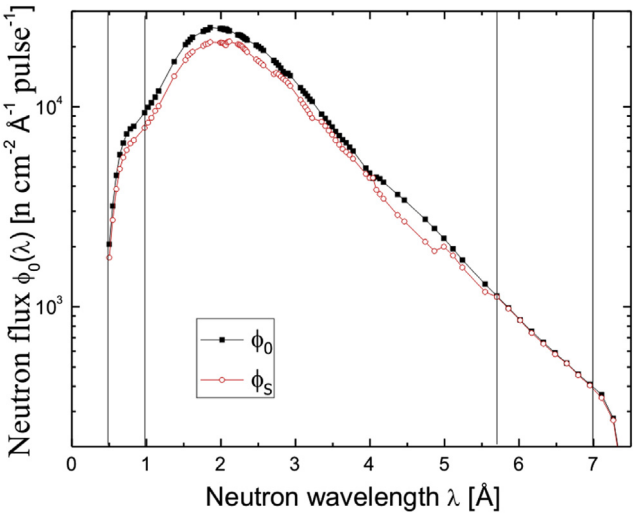

Fig. 9. Normalized neutron spectra for the Engin-X beamline measured with the MCP detector.

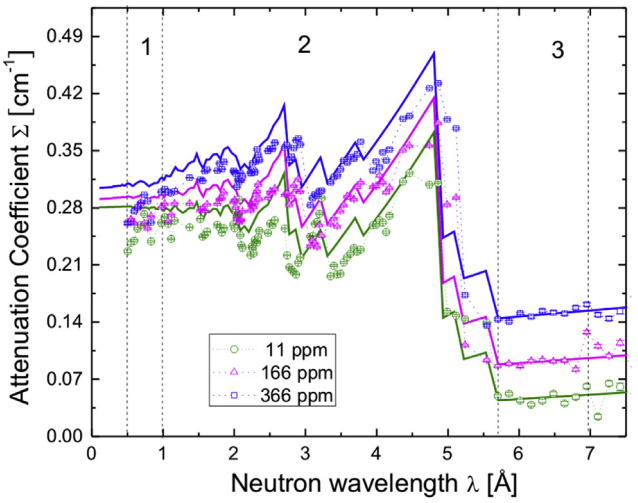

Fig. 10. Attenuation coefficient of three Zircaloy-2 calibration specimens measured on the Engin-X beamline with the MCP detector.

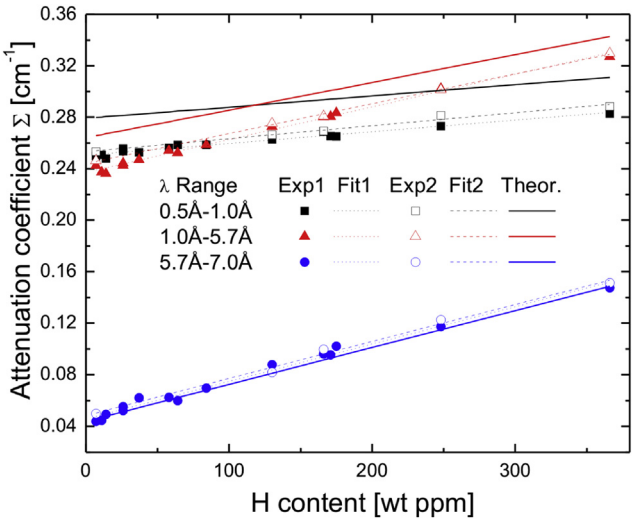

Fig. 11. Calibration lines for wavelength-resolved attenuation coefficients of Zircaloy-2 calibration specimens measured on the Engin-X beamline with the MCP detector.

theoretical estimations produced with Eq. (3) (solid lines). Overall, good qualitative agreement is observed, but quantitative agreement varies for different wavelength ranges (1,2,3), which we have identified by vertical dotted lines in the figure. A reasonable quantitative agreement is observed at intermediate wavelengths (region 2), where the attenuation coefficient is dominated by the Bragg edges resulting from coherent scattering on the crystal planes of the Zr lattice [23]. These differences are likely to be due to the crystallographic texture of the specimens. On the other hand, very good quantitative agreement is found at long wavelengths (region 3), where reflection on crystal planes is no longer possible (i.e., texture has no effect). Finally, a larger disagreement is found at short wavelengths (region 1), which could possibly be due to dead time effects of the detection system.

It is clear that the accuracy of the theoretical model (and hence the accuracy of the calibration) depends on the wavelength range used for recording the images. Hence, for the Engin-X experiments we have produced wavelength-selective attenuation coefficients, by adding the images corresponding to each of the regions identified in Fig. 10, respectively. Fig. 11 shows calibration lines obtained for the three wavelength intervals. Solid and open symbols are experimental values obtained on the first and second visit to the instrument, respectively. Dotted lines are calibration lines obtained from linear fits to the experimental data, and solid lines are calibration lines evaluated from the theoretical estimations described here. Table 4 lists the slopes and ordinates obtained for all cases. As expected, excellent agreement is obtained between experimental and theoretical calibration lines for region 3, whilst for regions 1 and 2 slopes are good, but the value of the ordinate has a shift of ~0.02 cm^{-1}.

This shows that wavelength-selective neutron imaging experiments using wavelengths longer than 5.7 Å can be effectively used to determine H contents in the 1–200 wt ppm range, without the need of calibration specimens. Moreover, by performing statistically sound measurement and adopting a theoretical calibration, a precision better than 1 wt ppm H is likely to be achieved. However, as neutron flux is low for these wavelengths (Fig. 9), counting times will increase in more than an order of magnitude.

11.3. Future prospects

Here we have determined the H content present in a Zr alloy component by ascribing the overall increase measured in the neutron attenuation coefficient of the Zr alloy material exclusively to the presence of H atoms. We have found that this is particularly robust for neutrons of wavelengths longer then 5.7 Å, but that for shorter wavelengths (1.5 Å -5Å) the attenuation coefficient may also change due to local microstructural changes such as the crystallographic texture of the metal lattice. So, in some situations it may be important to unequivocally assure the presence of H, in order to support or refine such determination. In this sense, analysis of the Zr hydride attenuation coefficient of Fig. 1 suggests two possible experimental measurement strategies that can be performed, in cases where the imaging instrument offers the capability of energy selection or discrimination. As displayed by the red line in Fig. 1, the first Bragg edge for the cubic structure of Zirconium hydride appears at 5.52 Å, whilst the edge for hexagonal structure of Zr appears at 5.61 Å. So, the presence of the hydride can be

Table 4
Theoretical and experimental parameters of the wavelength-dependent calibration lines.

Range [Å]	Engin-X, 1st		Engin-X, 2nd		Theoretical	
	Slope $d\bar{\Sigma}/dH$ (cm^{-1}/wt ppm H)	Ordinate $\bar{\Sigma}_0$ (cm^{-1})	Slope $d\bar{\Sigma}/dH$ (cm^{-1}/wt ppm H)	Ordinate $\bar{\Sigma}_0$ (cm^{-1})	Slope $d\bar{\Sigma}/dH$ (cm^{-1}/wt ppm H)	Ordinate $\bar{\Sigma}_0$ (cm^{-1})
0.5–7.5	$(2.2 \pm 0.2)10^{-4}$	0.238 ± 0.005	$(2.25 \pm 0.05)10^{-4}$	0.237 ± 0.001	2.1×10^{-4}	0.261
0.5–1.0	$(1.04 \pm 0.01)10^{-4}$	0.252 ± 0.001	$(1.08 \pm 0.01)10^{-4}$	0.259 ± 0.001	0.9×10^{-4}	0.279
1.0–5.7	$(2.60 \pm 0.01)10^{-4}$	0.236 ± 0.001	$(2.32 \pm 0.01)10^{-4}$	0.242 ± 0.001	2.2×10^{-4}	0.264
5.7–7.5	$(2.90 \pm 0.01)10^{-4}$	0.046 ± 0.001	$(2.87 \pm 0.01)10^{-4}$	0.048 ± 0.002	2.90×10^{-4}	0.044

confirmed by observation of the edge corresponding to the hydride. Another feature to be exploited is the oscillation displayed by the hydride at ~0.75 Å, which results from inelastic scattering by exchange of a 0.145 eV phonon [35].

As discussed in the introduction, the most interesting application of the present technique lies in its potential capability for in-situ quantification of H diffusion in fuel cladding or pressure tube material during DHC tests at operation temperatures. So it is worth discussing the effect of temperature on attenuation coefficients, in order to define the optimal experimental arrangement. At 330 °C H solubility in Zr alloys is ~115 wt ppm H [2], so for concentrations below this value H will be present as interstitials at the tetrahedral sites of the hexagonal Zr lattice rather than as constituents of the hydride phase. This could in principle produce considerable changes in the wavelength-dependent attenuation coefficient due to H, e.g., Σ_H(ZrH) (the red curve in Fig. 1). However, the vibrational movement of the H is almost identical in both cases, so the vibrational contribution to the attenuation coefficient (0.1 Å-1.5 Å range) does not change. On the other hand, differences are indeed expected for the diffusional movement of the proton when present either as an interstitial, or as part of the hydride crystal lattice structure. The impact of such differences in the attenuation coefficient has not yet been reported in the literature. On either form, the total cross section of H for wavelengths longer than 1.5 Å will strongly increase with temperature, due to the activation of inelastic scattering processes on which the neutron gains one or more phonons in the collision. For the threshold wavelength of 5.7 Å we estimate an increase by ~20% in the attenuation coefficient due to H at 350 °C, as compared to the room temperature value.

The techniques discussed here can in principle be extended to the determination of very low H contents in other metallic alloys; yet the sensitivity will depend on the actual attenuation coefficient of each alloy. In most cases, the best sensitivity is likely to be achieved for neutrons with wavelengths longer than the first Bragg edge of the metal matrix structure, as discussed in the previous section. For proper quantification, the wavelength-dependent attenuation coefficient for H in the chemical form present in the material (e.g. the red curve in Fig. 1) must be known by modeling or experiment.

12. Conclusions

- The capability of measuring very low H content in Zr alloys with a precision of ~5 wt ppm H and a spatial resolution of ~25 μm was demonstrated by using an adequate measurement protocol on a cold neutron imaging beamline.
- All neutron imaging instruments explored in this work can be effectively used for non-destructive evaluation of very low Hydrogen contents (0–300 wt ppm H) in Zr alloys, with varying spatial resolutions, dictated by the neutron beam divergence (L/D), and the available counting time.
- The effect of different experimental variables and characteristics of the specimen on the resolution and accuracy of the technique was explained, and several possibilities were proposed in order to improve resolution and avoid the use of calibration specimens.
- Wavelength-resolved neutron imaging experiments for wavelengths longer than 5.7 Å can be used to determine H content without the need of calibration experiments with a resolution better than 5 wt ppm H.
- Edge effects, affecting the maximum spatial resolution achievable by neutron imaging near interfaces, have been observed and minimized.
- It was found that the microstructure of the alloy has an important effect on the homogeneity of H across a specimen.

Acknowledgments

This research was funded by CONICET under PIP-11220110100542, by IAEA under Research Contract 17252, and by NSERC/UNENE Industrial Research Chair in Nuclear Materials at Queen's University. The authors thank CAB, MLZ, PSI and RAL for providing beam time at RA-6, ANTARES, ICON and Engin-X, respectively.

Appendix A. Supplementary data

Supplementary data related to this article can be found at https://doi.org/10.1016/j.jnucmat.2018.02.048.

References

[1] M.P. Puls, The Effect of Hydrogen and Hydrides on the Integrity of Zirconium Alloy Components, Springer London, London, 2012. http://link.springer.com/10.1007/978-1-4471-4195-2. (Accessed 12 August 2014).
[2] J.J. Kearns, Terminal solubility and partitioning of hydrogen in the alpha phase of zirconium, Zircaloy-2 and Zircaloy-4, J. Nucl. Mater. 22 (1967) 292–303, https://doi.org/10.1016/0022-3115(67)90047-5.
[3] J.J. Kearns, Diffusion coefficient of hydrogen in alpha zirconium, Zircaloy-2 and Zircaloy-4, J. Nucl. Mater. 43 (1972) 330–338, https://doi.org/10.1016/0022-3115(72)90065-7.
[4] IAEA, Delayed Hydride Cracking in Zirconium Alloys in Pressure Tube Nuclear Reactors, 2004. http://www-pub.iaea.org/books/IAEABooks/7007/Delayed-Hydride-Cracking-in-Zirconium-Alloys-in-Pressure-Tube-Nuclear-Reactors. (Accessed 28 March 2017).
[5] M. Kerr, M.R. Daymond, R.A. Holt, J.D. Almer, S. Stafford, K.B. Colas, Fracture of a minority phase at a stress concentration observed with synchrotron X-ray diffraction, Scripta Mater. 61 (2009) 939–942, https://doi.org/10.1016/j.scriptamat.2009.07.030.
[6] M. Kerr, M.R. Daymond, R.A. Holt, J.D. Almer, S. Stafford, Observation of growth of a precipitate at a stress concentration by synchrotron X-ray diffraction, Scripta Mater. 62 (2010) 341–344, https://doi.org/10.1016/j.scriptamat.2009.10.031.
[7] O. Zanellato, M. Preuss, J.-Y. Buffiere, F. Ribeiro, A. Steuwer, J. Desquines, J. Andrieux, B. Krebs, Synchrotron diffraction study of dissolution and precipitation kinetics of hydrides in Zircaloy-4, J. Nucl. Mater. 420 (2012) 537–547, https://doi.org/10.1016/j.jnucmat.2011.11.009.
[8] P. Vizcaíno, J.R. Santisteban, M.A. Vicente Alvarez, A.D. Banchik, J. Almer, Effect of crystallite orientation and external stress on hydride precipitation and dissolution in Zr2.5%Nb, J. Nucl. Mater. 447 (2014) 82–93, https://doi.org/10.1016/j.jnucmat.2013.12.025.
[9] D. Khatamian, Deuterium diffusion along the three principal directions in anisotropic Zr–2.5Nb, J. Alloy. Comp. 580 (1) (2013) S58–S62, https://doi.org/10.1016/j.jallcom.2013.03.016.

[10] N.L. Buitrago, Advanced Neutron Imaging Techniques on Zr-Alloy Components, Ph D Thesis, Insituto Balseiro, Bariloche, Argentina, 2018 (In Spanish).
[11] A. Zeilinger, W.A. Pochman, New method for the measurement of hydrogen diffusion in metals, J. Appl. Phys. 47 (1976) 5478–5479, https://doi.org/10.1063/1.322544.
[12] R. Yasuda, M. Nakata, M. Matsubayashi, K. Harada, Y. Hatakeyama, H. Amano, Application of hydrogen analysis by neutron imaging plate method to Zircaloy cladding tubes, J. Nucl. Mater. 320 (2003) 223–230, https://doi.org/10.1016/S0022-3115(03)00112-0.
[13] E.H. Lehmann, P. Vontobel, N. Kardjilov, Hydrogen distribution measurements by neutrons, Appl. Radiat. Isot. 61 (2004) 503–509, https://doi.org/10.1016/j.apradiso.2004.03.075.
[14] M. Grosse, E. Lehmann, P. Vontobel, M. Steinbrueck, Quantitative determination of absorbed hydrogen in oxidised zircaloy by means of neutron radiography, Nucl. Instrum. Methods Phys. Res. Sect. Accel. Spectrometers Detect. Assoc. Equip 566 (2006) 739–745, https://doi.org/10.1016/j.nima.2006.06.038.
[15] M. Grosse, M. van den Berg, C. Goulet, E. Lehmann, B. Schillinger, In-situ neutron radiography investigations of hydrogen diffusion and absorption in zirconium alloys, Nucl. Instrum. Methods Phys. Res. Sect. Accel. Spectrometers Detect. Assoc. Equip 651 (2011) 253–257, https://doi.org/10.1016/j.nima.2010.12.070.
[16] J.R. Granada, J.R. Santisteban, R.E. Mayer, Non-destructive determination of very low hydrogen content in metals with the use of neutron techniques, Phys. B Condens. Matter 213–214 (1995) 1005–1007, https://doi.org/10.1016/0921-4526(95)00349-E.
[17] K. Beyer, T. Kannengiesser, A. Griesche, B. Schillinger, Study of hydrogen effusion in austenitic stainless steel by time-resolved in-situ measurements using neutron radiography, Nucl. Instrum. Methods Phys. Res. Sect. Accel. Spectrometers Detect. Assoc. Equip 651 (2011) 211–215, https://doi.org/10.1016/j.nima.2011.02.010.
[18] A. Couet, A.T. Motta, R.J. Comstock, Hydrogen pickup measurements in zirconium alloys: relation to oxidation kinetics, J. Nucl. Mater. 451 (2014) 1–13, https://doi.org/10.1016/j.jnucmat.2014.03.001.
[19] W.L. Whittemore, A.W. McReynolds, Effects of chemical binding on the neutron cross section of hydrogen, Phys. Rev. 113 (1959) 806–808, https://doi.org/10.1103/PhysRev.113.806.
[20] J.R. Santisteban, M.A. Vicente-Alvarez, P. Vizcaino, A.D. Banchik, S.C. Vogel, A.S. Tremsin, J.V. Vallerga, J.B. McPhate, E. Lehmann, W. Kockelmann, Texture imaging of zirconium based components by total neutron cross-section experiments, J. Nucl. Mater. 425 (2012) 218–227, https://doi.org/10.1016/j.jnucmat.2011.06.043.
[21] M. Grosse, M. Steinbrueck, A. Kaestner, Wavelength dependent neutron transmission and radiography investigations of the high temperature behaviour of materials applied in nuclear fuel and control rod claddings, Nucl. Instrum. Methods Phys. Res. Sect. Accel. Spectrometers Detect. Assoc. Equip 651 (2011) 315–319, https://doi.org/10.1016/j.nima.2011.02.102.
[22] J.R. Santisteban, Desarrollo de nuevas técnicas neutrónicas para el estudio experimental del Sistema Metal-Hidrógeno, Instituto Balseiro, Universidad Nacional de Cuyo, 1998.
[23] E. Fermi, W.J. Sturm, R.G. Sachs, The transmission of slow neutrons through microcrystalline materials, Phys. Rev. 71 (1947) 589–594, https://doi.org/10.1103/PhysRev.71.589.
[24] R. Woracek, J. Santisteban, A. Fedrigo, M. Strobl, Diffraction in neutron imaging–A review, Nucl. Instrum. Methods Phys. Res. Sect. Accel. Spectrometers Detect. Assoc. Equip. (n.d.). doi:10.1016/j.nima.2017.07.040.
[25] A.V. Flores, A.G. Gomez, G.A. Juarez, N. Loureiro, R.I. Samper, J.R. Santisteban, M.A.V. Alvarez, A. Tolley, A. Condó, R.D. Bianchi, A.D. Banchik, P. Vizcaíno, Typical zirconium alloys microstructures in nuclear components, Pract. Metallogr. 51 (2014) 656–674, https://doi.org/10.3139/147.110304.
[26] C.E. Ells, Hydride precipitates in zirconium alloys (A review), J. Nucl. Mater. 28 (1968) 129–151, https://doi.org/10.1016/0022-3115(68)90021-4.
[27] E. Calzada, F. Gruenauer, M. Mühlbauer, B. Schillinger, M. Schulz, New design for the ANTARES-II facility for neutron imaging at FRM II, Nucl. Instrum. Methods Phys. Res. Sect. Accel. Spectrometers Detect. Assoc. Equip 605 (2009) 50–53, https://doi.org/10.1016/j.nima.2009.01.192.
[28] J. Marín, F. Sanchez, H. B, Rediseño construcción y caracterización de la nueva instalación de neutrografía del RA-6, Rev. CNEA 49–50 (2013) 5–10.
[29] J.R. Santisteban, M.R. Daymond, J.A. James, L. Edwards, ENGIN-X: a third-generation neutron strain scanner, J. Appl. Crystallogr. 39 (2006) 812–825, https://doi.org/10.1107/S0021889806042245.
[30] A.S. Tremsin, J.B. McPhate, J.V. Vallerga, O.H.W. Siegmund, J.S. Hull, W.B. Feller, E. Lehmann, Detection efficiency, spatial and timing resolution of thermal and cold neutron counting MCP detectors, Nucl. Instrum. Methods Phys. Res. Sect. Accel. Spectrometers Detect. Assoc. Equip 604 (2009) 140–143, https://doi.org/10.1016/j.nima.2009.01.041.
[31] A.P. Kaestner, S. Hartmann, G. Kühne, G. Frei, C. Grünzweig, L. Josic, F. Schmid, E.H. Lehmann, The ICON beamline – a facility for cold neutron imaging at SINQ, Nucl. Instrum. Methods Phys. Res. Sect. Accel. Spectrometers Detect. Assoc. Equip 659 (2011) 387–393, https://doi.org/10.1016/j.nima.2011.08.022.
[32] M. Grosse, C. Roessger, J. Stuckert, M. Steinbrueck, A. Kaestner, N. Kardjilov, B. Schillinger, Neutron imaging investigations of the secondary hydriding of nuclear fuel cladding alloys during loss of coolant accidents, Phys. Procedia 69 (2015) 436–444, https://doi.org/10.1016/j.phpro.2015.07.061.
[33] P. Trtik, E.H. Lehmann, Progress in high-resolution neutron imaging at the Paul scherrer Institut - the neutron microscope project, J. Phys. Conf. Ser 746 (2016) 012004, https://doi.org/10.1088/1742-6596/746/1/012004.
[34] L. Barrow, A.T.W. Barrow, J. Almer, M.R. Daymond, The Zr20Nb–H phase diagram and the characterisation of hydrides in β-Zr, J. Nucl. Mater. 442 (2013) 292–297, https://doi.org/10.1016/j.jnucmat.2013.08.031.
[35] D.E. Parks, et al., Slow Neutron Scattering and Thermalization with Reactor Applications, Addison Wesley Longman, New York, 1970.